Chapter 6

Magnetic properties and coupled spin-phonon behavior in quasi one-dimensional screw-chain compound $BaMn_2V_2O_8$

6.1. Introduction:

The study of low dimensional magnetic systems has started seeking immense attention globally due to their intriguing rich magnetic phenomena [140], [263], [264]. They also hold promise for their potential applications in quantum computation [264]. The topology and dimensionality of such a spin system as well as its interactions occurring with other microscopic order parameters, such as lattice, phonon, charge, and orbital degrees of freedom, have a profound influence on its various aspects. In this regard, the research on 1D spin-chain systems has been a very active field of experimental as well as the theoretical condensed matter physics. In a perfect 1D AFM spin system, the persistence of the strong thermal and quantum fluctuations at low temperatures, which are triggered by the macroscopic degeneracy destroys the LRO, leading to the well-known exotic phenomenon of spin liquid. Nevertheless, a real quasi-1D AFM spin system can exhibit a spin liquid state, or a 3D Néel-type or an XY-type magnetic ordering, which depends on various factors such as the interchain interactions, magnetic anisotropy, and also spin values [38], [126], [143]. In fact, the half-integer spin chain systems are gapless, wherein finite interchain interactions lead to the LRO. On the contrary, an integer spin-chain system may exhibit a spin gap by showing a singlet ground state and triplet excited states, which manifest in their behavior as a nonmagnetic substance at low temperatures.

In this context, a series of compounds having a chemical formula $AM_2V_2O_8$ (where, A=Ba, Sr, Pb; and M= Co, Mn, Ni, Cu) have attracted much interest owing to their distinct structures and varied intriguing magnetic properties. One general structural feature of this series of compounds is that it consists of arrays of edge-shared $M^{2+}O_6$ octahedra forming screw-chains along the crystallographic *c*-axis, leading to a quasi-1D structural arrangement of magnetic ions (M). Such magnetic screw-chains are separated by the nonmagnetic tetrahedra of $V^{5+}O_4$ and also nonmagnetic A^{2+} ions. Despite having similar

crystal structures (although with different crystal symmetries), various $AM_2V_2O_8$ compounds display solely distinct magnetic properties, which vary with a change in the magnetic ions from Cu^{2+} to Mn^{2+}. As a matter of fact, the isolated spin dimer or alternating spin-chain system $BaCu_2V_2O_8$ shows a large spin gap with a singlet ground state [51]; the honeycomb magnetic system $BaNi_2V_2O_8$ shows a quasi-two-dimensional (2D) AFM ordering (XY-type) with dominant easy-plane anisotropy [133]; whereas the Haldane-gap spin-chain AFM systems, $SrNi_2V_2O_8$ and $PbNi_2V_2O_8$ exhibit interesting quantum critical phase transition that lies between the spin liquid and Ising-like magnetic states [128]. On the other hand, the Ising spin systems with strong magnetic anisotropy, viz., $BaCo_2V_2O_8$, $PbCo_2V_2O_8$, and $SrCo_2V_2O_8$ compounds display interesting field-driven quantum phase transition [52], [139], [141]. On the contrary, S=5/2 spin-chain compounds $SrMn_2V_2O_8$ (T_N~42.2 K) and BMVO (T_N~38 K) exhibit long-range AFM ordering at relatively much higher temperatures as compared to the other compounds in the aforementioned series [131], [144]. Although the magnetic structure of the LRO system $SrMn_2V_2O_8$ was revealed previously [131], the spin structure of the BMVO system is still unknown, which prompted us to carry out an NPD study on the BMVO compound in the present study.

On the other hand, SPC is a fascinating phenomenon of condensed matter physics that ensues from the mutually coupled spin and phononic order parameters. In such a process, the thermal evolution of phonon spectra of a system exhibiting SPC demonstrates anomalous phonon modulation near the magnetic ordering temperature. The SPC can also be a useful gauge for probing various intriguing phenomena, which include the magnetostriction effect, spin Seebeck effect, thermal Hall effect, spin-Peierls transition, magnetoelectric effect, etc [265], [266].

Moreover, the $AM_2V_2O_8$ compounds have been extensively studied mainly for their magnetic properties, whereas their other physical properties are not much explored.

Regardless of the strong interactions between the lattice vibration and magnetism, the studies exploring the SPC remained largely undiscovered in the spin-chain materials. However, the existence of the spin-lattice coupling and magnetoelectric effect has been recently reported in spin-chain compounds $NiTe_2O_5$ and Tb_2BaNiO_5 [267], [268]. Eventually, such phenomena are often interlinked with an SPC effect following the Lyddane-Sachs-Teller (LST) relation [269]. Thus, it may be interesting to study the temperature-dependent Raman spectroscopy of BMVO, which can probe the lattice dynamics behavior, especially near the T_N. Moreover, the relatively higher T_N of the BMVO system as compared to the other similar spin-chain materials renders it a unique playground for studying the SPC phenomenon in this system, which is hitherto unreported.

6.2. Experimental and computational methods:

A polycrystalline sample of BMVO was synthesized following a standard solid-state reaction method. High-purity oxide powders (>99.99%, Alfa-Aesar) of $BaCO_3$, MnO, and V_2O_5 as starting materials were taken in a proper stoichiometric ratio, which was followed by a mixing and intimate grinding for an hour. The mixture was pressed into pellets and thereafter, they were subjected to several heating cycles with intermediate grindings at 750 and 840 °C for 48 h (at each cycle) under flowing of Ar-gas. The purity of the crystal phase of the final product was verified by the XRD. The XRD data at 300 K was recorded using a D8 Advance Bruker diffractometer with Cu-$K\alpha_1$ radiation. All the magnetization measurements were performed utilizing a SQUID-based magnetometer (MPMS, Quantum Design). Temperature-dependent micro-Raman spectroscopy data were collected using a single-frequency Nd: YVO_4 laser (DPSS series by Lasos) having an excitation wavelength of 532.2 nm. The data were recorded in back-scattering geometry with the help of a monochromator ACTON SP750, which is equipped with a 1200 groove mm^{-1} grating. XAS data were collected in a TEY mode at the BL20 beamline of the National Synchrotron

Radiation Research Centre (NSRRC), Taiwan. The neutron diffraction measurements were carried out by the PD2 neutron powder diffractometer (λ =1.2443 Å) placed at the Dhruva reactor in Bhaba Atomic Research Centre (BARC), Mumbai, India. The *ab initio* DFT calculations were carried out utilizing the Vienna *ab initio* simulation package (VASP 6.1.2) using the PAW pseudo-potentials.

6.3. Results and discussions:

6.3.1. X-ray diffraction study:

Fig. 6.1 depicts the XRD pattern along with its Rietveld refinement of BMVO at 300 K. A Fullprof suite program has been used for performing the aforesaid structural analysis. The refinement of BMVO suggests a single-phase tetragonal structure with $I4_1cd$ symmetry (no. 110). No trace of any additional impurity peak is found, thus suggesting the pure phase formation of the sample. The obtained lattice parameters are a=b=12.612841 (10) Å and c = 8.663881 (10) Å, which are in good agreement with the previous report [270]. The detailed crystal structure has been demonstrated in the following section.

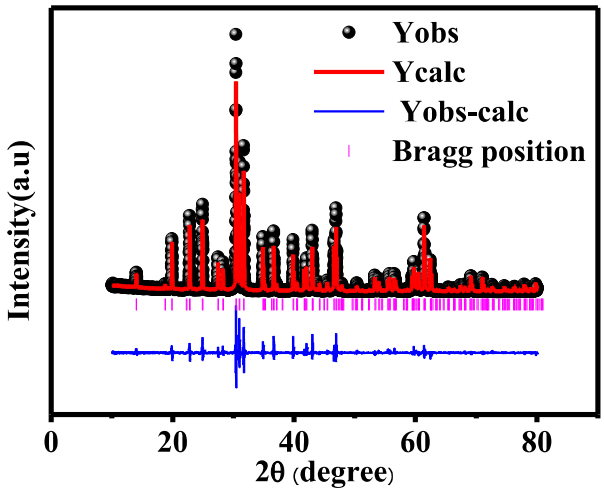

Fig. 6.1: Rietveld refinement of XRD pattern collected at room temperature (300 K) for BMVO.

6.3.2. Neutron diffraction study:

Furthermore, the NPD of BMVO has been performed at various temperatures to understand the microscopic spin structure as well as the crystal structure. The Rietveld refinement of the NPD pattern collected at 300 K is shown in Fig. 6.2(a). All the NPD data down to 40 K were fitted solely with the nuclear structure with symmetry $I4_1cd$. Fig. 6.2(c) to (g) demonstrate the crystal structure of BMVO as obtained from the NPD pattern (at 300 K) analysis. Fig. 6.2(c) shows the unit-cell, where the MnO_6 octahedra are shown in the *ab* plane. The basic polyhedral building blocks of the structure include a cuboctahedron of BaO_{12} (Fig. 6.2(e)), 6-fold oxygen coordinated MnO_6 octahedron, (Fig. 6.2(f)), and a tetrahedron of VO_4 (Fig. 6.2(g)). However, the aforesaid polyhedral blocks are slightly distorted, which is evident from the differences in various Ba-O, Mn-O, and V-O bond lengths (Fig. 6.2(e) to (g)). In this structure, the quasi-linear 1D chain is formed by edge-sharing MnO_6 octahedra, which creates a screw chain along the *c*-axis expressed by the 4_1-screw symmetry axis (Fig. 6.2(d)). There are four such spin-chains (screw) in a unit-cell that are centred at (0.25, 0.25, z), (0.25, 0.75, z), (0.75, 0.25, z), and (0.75, 0.75, z) on the *ab* plane. In BMVO, along a chain, the Mn-Mn distance is found to be around ~3 Å, whereas the distance between two chains (in the same *ab* plane) is around 6.6 Å. However, the minimum distance between two screw chains is ~5.16 Å, for which the two Mn ions are situated in two different *ab* planes separated by a distance of *c*/4. Therefore, the predominant magnetic interactions are expected to occur along the chain, while various weaker interchain superexchange interactions of similar strengths can take place via non-magnetic VO_4 tetrahedra.

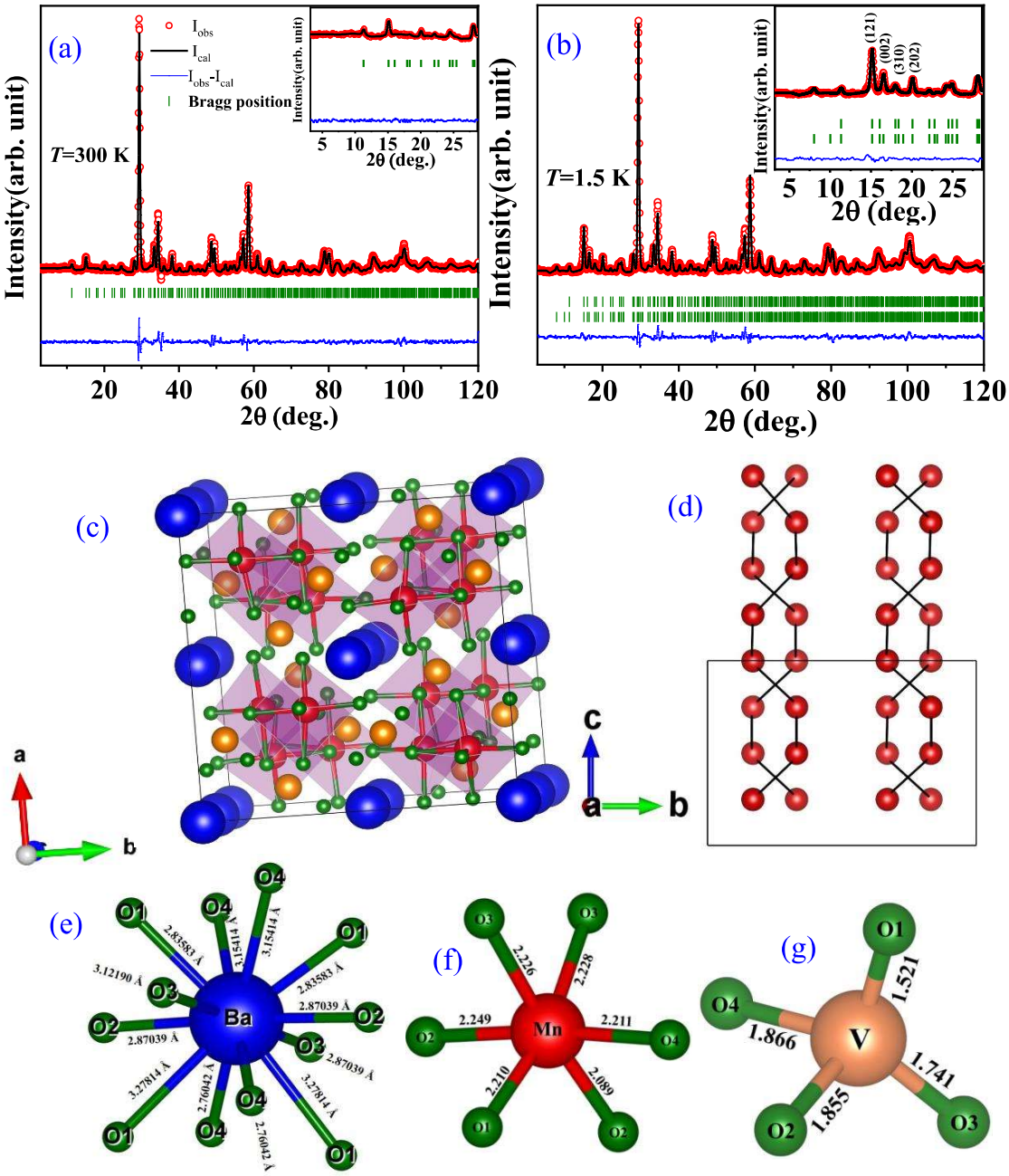

Fig. 6.2: (a) and (b) show the NPD data along with their Rietveld refinements at 300 and 1.5 K, respectively. The insets of (a) and (b) show the close views of the aforesaid plots at a lower angle ($2\theta<27^0$), thus showing the appearance of magnetic reflections for the data at 1.5 K. (c) The pictorial representation of the unit cell. (d) Represents a one-dimensional quasi-linear chain formed by edge-sharing MnO_6 octahedra which creates a screw-chain along the *c*-axis expressed by the 4_1-screw symmetry axis. (e) Cuboctahedron of BaO_{12}. (f) MnO_6 octahedra, (g) VO_4 tetrahedron.

Furthermore, in the temperature-dependent NPD patterns, an emergence of a new set of magnetic Bragg reflections (such as (002) and (310) near 2θ~16.5^0 and 18^0 respectively) as well as a drastic enhancement in some existing nuclear Bragg peaks (which include (121)/(211) near 2θ ~15^0 and (202)/(022) near 2θ~20^0) are observed below 40 K, which are evident from Fig. 6.3(a). The appearance of new magnetic Bragg reflections and also sudden rise in the intensities of some existing Bragg peaks (as mentioned above) can be evidenced more clearly from the corresponding "color-coded contour plot of the intensities of various NPD peaks as a function of temperature and 2θ", which has been shown in Fig. 6.3(b). This clearly suggests an onset of a long-range magnetic ordering below 40 K. The positions of the additional magnetic peaks (having (*hkl*) such that the value of *h*+*k*+*l* is an even integer) are also allowed by the body-centered (*I*) symmetry of the lattice, however, they are not allowed by the space group symmetry $I4_1cd$. Therefore, the NPD patterns below 40 K could not be fitted with nuclear structure alone, instead, an additional contribution from magnetic ordering was also included using a propagation vector k = (0, 0, 0) with respect to the tetragonal symmetry. All the peaks were satisfactorily indexed with the aforementioned combination fitting, which can be seen in Fig. 6.2(b) showing the NPD pattern at 1.5 K along with its Rietveld refinement. The unit-cell lattice constants, bond lengths, bond-angles, etc. as estimated from the NPD data refinement are summarized in Table 6.1.

Table 6.1: Structural parameters of BMVO as determined from the Rietveld refinement of the NPD data at *T*=1.5 K and 300 K with Space group: $I4_1cd$

Parameters	*T*=1.5 K	*T*=300 K
a=b (Å)	12.5980	12.6287
c (Å)	8.6571	8.6745
Ba	8a	8a
x	0.0000	0.0000
y	0.0000	0.0000
z	0.0000	0.0000
B_{iso} (Å^2)	0.5000	0.5000
Mn	16b	16b
x	0.3352(13)	0.3284(17)
y	0.3281(10)	0.3375(12)
z	0.252(3)	0.255(4)
B_{iso} (Å^2)	0.51(13)	0.55(16)
V	16b	16b
x	0.25302	0.25302
y	0.07669	0.07669
z	0.11128	0.11128
B_{iso} (Å^2)	0.43110	0.43146
O(1)	16b	16b
x	0.1625(10)	0.1606(10)
y	0.5070(9)	0.5050(9)
z	0.0471(16)	0.0476(19)
B_{iso} (Å^2)	0.63(16)	0.39(12)
O(2)	16b	16b
x	0.3565(9)	0.3564(9)
y	0.6708(12)	0.6708(12)
z	0.5183(16)	0.516(2)
B_{iso} (Å^2)	1.3(2)	1.2(3)
O(3)	16b	16b
x	0.1653(8)	0.1669(8)
y	0.6784(8)	0.6822(9)
z	0.7572(15)	0.750(2)
B_{iso} (Å^2)	0.22(11)	0.14(15)
O(4)	16b	16b
x	0.3400(6)	0.3380(11)
y	0.4958(7)	0.4979(8)
z	0.2338(18)	0.236(2)
B_{iso} (Å^2)	-0.23(11)	0.77(14)
R_{wp}	6.60	6.67
GOF	1.72	2.00
χ^2	5.83	6.79

The spin structure as obtained from the NPD data (at 1.5 K) analysis has been schematically shown in Fig. 6.3(c). The magnetic spins are parallel to each other on the *ab* plane, however, along the c-axis (along the screw-chain) the spins are antiparallel to each other. Therefore, if viewed along the *c*-axis, the spin arrangement will appear as a collinear AFM structure (considering the spins oriented along the *a*-axis), which is shown in Fig. 6.3(d). The best fit is obtained while a spin structure is considered, in which the spins are aligned perpendicular to the *c*-axis, i.e., they are either along the *a* or *b*-axis, while the moments along the other directions are considered to be zero or very weak. However, the precise determination of the moment direction along *a* or *b*-axis cannot be done with the presented NPD patterns, as they are not in a feasible range. Nevertheless, it confirms that the spins are entirely on the *ab*-plane.

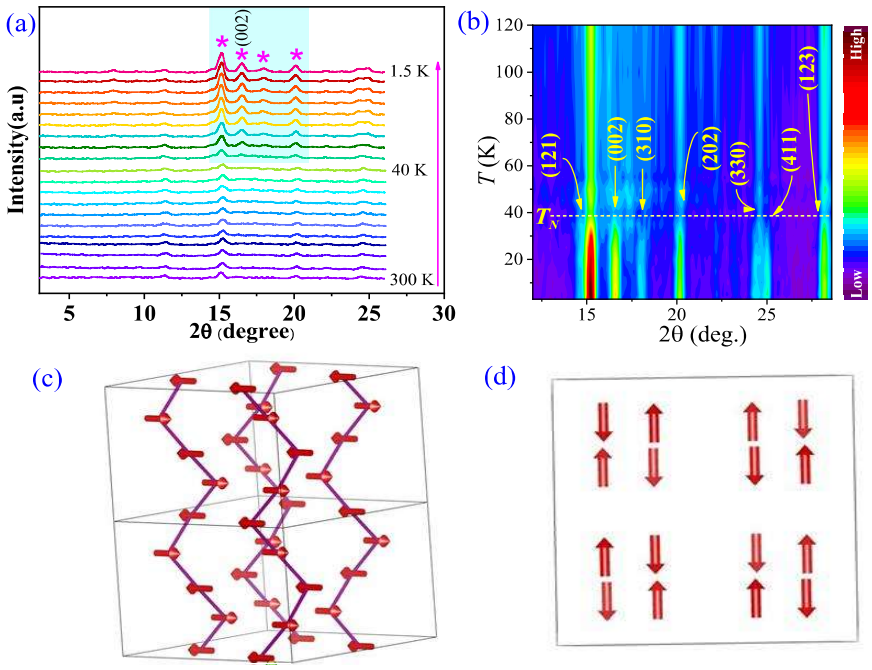

Fig. 6.3: (a) NPD patterns at different temperatures. The shaded region shows the onset of magnetic reflections below 40 K, (b) Color-coded contour plot of the intensity of NPD peaks (related to magnetic ordering) as a function of temperature and angle (2θ). Various Bragg reflections (*h k l*) are indicated in the figure below T_N~38 K. (c) Shows the microscopic magnetic structure of BMVO as determined from NPD data analysis. (d) A view of the spin structure as seen along the *c*-axis.

Moreover, the thermal variation of the magnetic moment of Mn^{2+} ions/site as determined from the NPD data analysis shows a sudden jump below 40 K and it attains merely a saturation at lower temperatures, which can be seen from Fig. 6.4(a). The refined magnetic moment of Mn^{2+} ions/site at 1.5 K is ~2.446 μ_B/Mn^{2+}, whereas the theoretically expected spin-only magnetic moment of completely saturated Mn^{2+} ions is 5.91 μ_B (S=5/2). The large suppression in the moment value can be presumably attributed to the existence of strong quantum fluctuations owing to the quasi-1D nature of the present system, which hinders the spins to attain a fully ordered state.

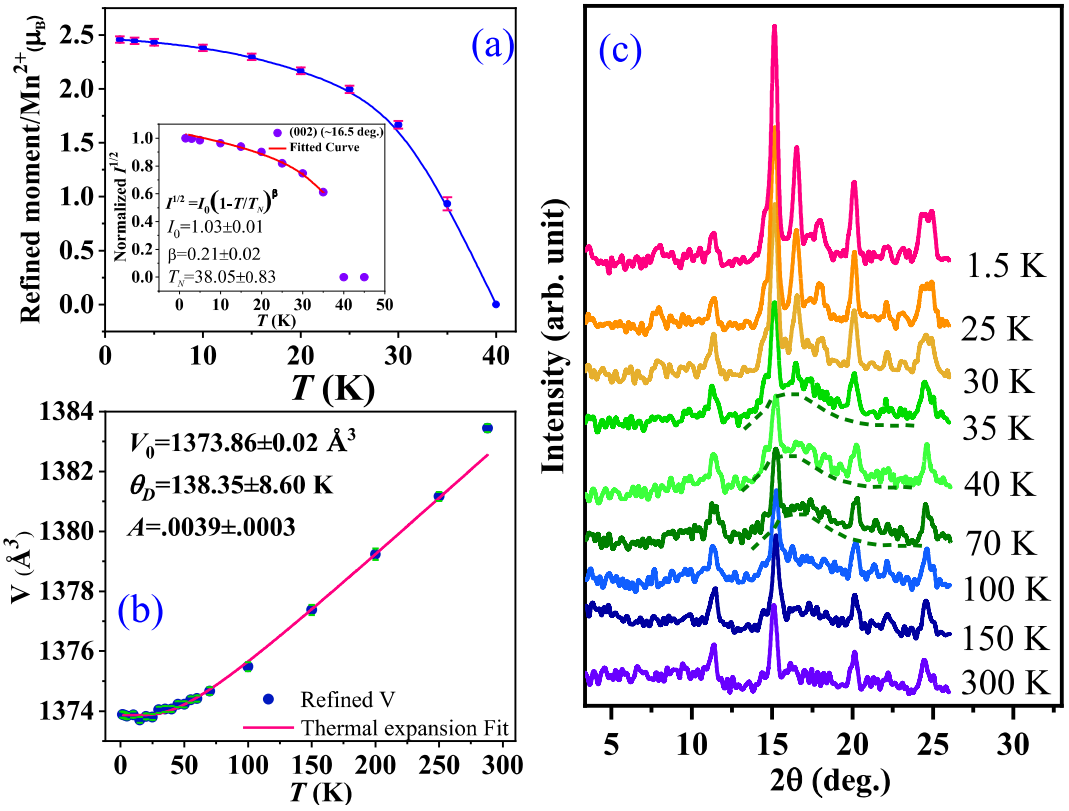

Fig. 6.4: (a) Temperature variation of the refined magnetic moment of Mn^{2+}/site. Inset of (a): Power law fitting of the normalized intensity of peak (002). (b) "Unit-cell volume (V) *vs.* T" plot along with its thermal expansion fit. (c) Shows the raw NPD data at some selected temperatures, in which the broad hump-like feature (diffusion) around 2θ ~12 to 25^0 (as indicated by the dotted green-line for the data at 35, 40, and 70 K) is visible for the data in between 25 K and 300 K.

Furthermore, we have performed a critical exponent analysis on a selective magnetic reflection (002), which is the most prominent peak that appeared only below 40 K (Fig. 6.3(a) and (b)). The inset of Fig. 6.4(a) demonstrates the temperature dependence of the normalized "square-root" of the intensity (I) of (002) reflection peak, wherein the normalization is done with respect to the peak at 1.5 K. A Gaussian-function fit has been employed to estimate the normalized intensity of the peaks (002) at various temperatures. It is found that the positions of the (002) peaks remain unaltered with lowering the temperature, thus confirming the k to be uniform down to 1.5 K. In the case of a magnetic phase transition at T_N from a PM state to an LRO (AFM) state, the ordered moment (m) can be expressed as $m \propto (T_N\text{-}T)^{\beta}$. On the other hand, m and I are related to each other as follows: $m \propto \sqrt{I}$. Therefore, $\sqrt{I(T)} = I_0(T - T_N)^{\beta}$; where I_0 is a proportionality constant, T_N is the ordering temperature, and β is the order parameter of the critical exponent, the value of which can suggest the nature of the magnetic ordering. The inset of Fig. 6.4(a) demonstrates the power law fitting (in accordance with the aforementioned relation) of "$\sqrt{I}$ *vs. T"* curve for (002) magnetic reflection. The fitting was satisfactory, which yielded T_N =38.05 ± 0.83 K and β=0.21 ± 0.02. According to the dimensions of space and spins, magnetic systems are classified into several categories with different values of β, such as β=0.125 indicates 2D Ising; β=0.33 implies 3D Ising; β=0.35 signifies 3D XY; β=0.36 suggests 3D Heisenberg, and β=0.5 indicates mean-field model. Therefore, the estimated value of β=0.21 for BMVO lies in an intermediate regime, i.e., in between the 2D Ising and the other aforementioned classes. Nevertheless, the observations of such smaller values of β in other systems are not rare, as many works had reported such unconventional values, including recent work on a 1D spin-chain system $NiTe_2O_5$ [268], [271], [272].

As previously mentioned, no global structural phase transition in BMVO is observed down to 1.5 K, as all the data has been satisfactorily fitted with the $I4_1cd$ symmetry along with

magnetic contribution with k=(0, 0, 0). The variation of unit-cell volume (V) as a function of temperature is shown in Fig. 6.4(b). No remarkable anomaly has been observed throughout the temperature range of our study. The V of a system typically follows thermal relaxation behavior, which is described as:

$$V(T) = V_0\left[1 + \frac{A}{\left(e^{\frac{\theta_D}{T}} - 1\right)}\right]; \qquad 6.1$$

Here, V_0 is the lattice constant at 0 K, while A is an adjustable parameter of the fitting and θ_D represents the Debye temperature. It is observed that the *V(T)* curve closely follows the thermal expansion law in the range 250 to 1.5 K. A small deviation is observed just above 250 K. A local structural distortion may be an underlying reason for the observed deviation. However, due to the lack of more data points above 250 K, it cannot confirm the local distortion in the structure. On the other hand, our Raman spectroscopy study also showed an anomalous phonon behavior in the vicinity of 250 K, which will be discussed in the following section.

Moreover, NPD measurements are also capable of sensing magnetic SRO in a system, in which the diffuse scattering related to the SRO typically occurs above T_N around the same position in the reciprocal plane, where the magnetic superlattice reflection emerges in LRO below T_N [273]. In fact, the diffused peaks can be originated from the magnetic or atomic SRO (disorder), as it gives rise to the isotropic background owing to the modified form factor. Generally, the diffused patterns produced at low angles, i.e., below $2\theta=20^0$, are typical of magnetic origin and the contribution from the atomic SRO (by the thermal vibrations) is negligible in this case [274]. On the other hand, in general, above $2\theta=30^0$, the diffused peaks are of entirely atomic origin [274]. For the case of BMVO, Fig. 6.4(c) displays the raw NPD data at some selected temperatures as indicated in Fig. to avoid

complexity. It is observed that a broad hump-like feature (as marked by the green dotted line for the data at 35, 40, and 70 K) in the range of 2θ~12-25^0 is discernible for the NPD patterns at temperatures above 25 K. The feature becomes more prominent as the temperature cools below 100 K down to 25 K, whereas it gets suppressed but still is present in the NPD data at least up to 200 K (not shown). As the temperature is lowered below T_N, the diffused scattering starts transforming into a set of Bragg peaks and upon further lowering the temperature below around 25 K, the broad feature almost merges with the Bragg peaks. Thus, this is an indication of the existence of an SRO above and also below its T_N and it persists at least up to 200 K. The existence of the diffused scattering even below T_N indicates that the LRO takes place gradually in a wide temperature range and the phase transition is not sharp immediately below its T_N. Such coexistence of SRO in the LRO state T_N is not rare in the low dimensional and frustrated magnetic systems [131], [275]. In such low dimensional spin-chain systems, as the temperature is cooled, the SRO emerges when the strength of the intrachain interactions becomes comparable to the thermal energy. However, as the temperature is lowered further below T_N, the thermal energy becomes comparable to the interchain interactions (weaker) as well and thereafter a 3D LRO is established in the system. In fact, the thermal variation of dc magnetization data also suggested the existence of SRO in BMVO, which will be discussed in the following section.

6.3.3 X-ray Absorption Spectra study:

Prior knowledge of the electronic structure of a system helps in understanding its magnetic property. The XAS technique is a unique and powerful tool to probe the oxidation states of various ions. Thus, we recorded the XAS spectra in a TEY mode for the system under study. The multiplet structure of the Mn*2p* XAS spectra at the $L_{2\text{-}3}$ edge of BMVO, as well as a standard reference sample MnO, have been collected at 300 K, which are shown in

Fig. 6.5. Both the Mn*2p* XAS spectra consist of two main spin-orbit splitting peaks, i.e., Mn$2p_{3/2}$ (MnL_3) at ~640.6 eV and Mn$2p_{1/2}$ (MnL_2) at ~651.2 eV. Again, each peak is further split into two due to the crystal field effect. The close match between the line shapes, peak positions, and doublet separations of both the XAS spectra clearly suggest a nominal valence state of +2 for Mn ions in BMVO. No trace of mixed valence states is found in this system.

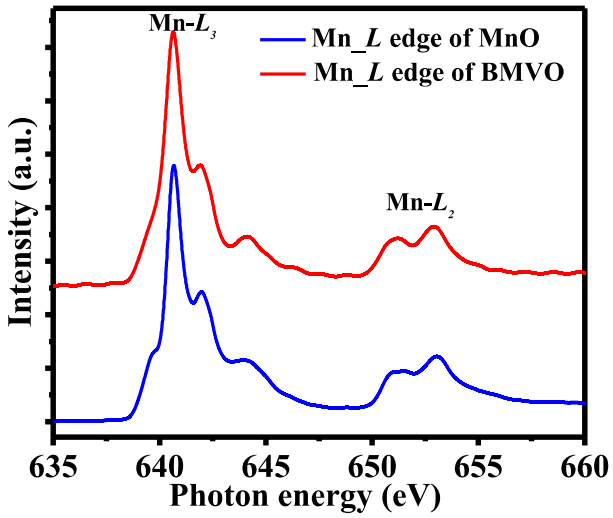

Fig. 6.5: The XAS spectra of Mn ions with Mn L_2 edge and Mn L_3 edge of BMVO along with the comparison of Mn L-edge spectra of MnO compound.

6.3.4 Magnetization study:

Fig. 6.6(a) displays the temperature variation of the dc magnetization curves i.e., $M(T)$ curves recorded under a magnetic field of 2 T, following the standard ZFC and FC methods. The $M(T)$ curves show an increase in M with decreasing temperature, thereby attaining a plateau nearly below 170 K. However, upon further cooling, as temperature goes nearly beyond ~120 K, the M starts increasing again, thereafter it exhibits an upturn closely below

~100 K, which may seemingly be attributed to the enhanced SRO in the system, as it was also previously suggested by the NPD data. Moreover, the exhibition of the plateau by the $M(T)$ curves below around 170 K is a typical feature of a low-dimensional system. However, on further cooling of the temperature below T_N=38 K, the $M(T)$ curves show a sudden jump, thus manifesting an LRO AFM transition around this temperature. The observed T_N (~38 K) is slightly higher than the previously reported magnetic transition temperature of this system, which was 37 K [144]. Fig. 6.6(b) shows the corresponding plot (FC) of the "inverse susceptibility (χ^{-1}) *vs. T"* curve. It clearly shows deviation from the linearity even at temperatures much higher than T_N. Thus, it violates the CW law (which is given by: $\chi = \frac{C}{T-\theta_{CW}}$, where C denotes the Curie constant and Θ_{CW} represents the CW temperature) even at the elevated temperatures, which can be presumably attributed to the SRO prevailing above T_N. However, a linear behavior of $\chi^{-1}(T)$ curve is observed above ~240 K, thus, a CW fit has been performed in a relatively narrow temperature range of 240-300 K. The fitting yielded μ_{eff} =6.306 μ_B/Mn^{2+} and Θ_{CW} =-464.08 K. However, the theoretically calculated spin-only moment of Mn^{2+} ions (S=5/2) is μ_{theo}=5.92 $\mu_B//Mn^{2+}$, which is slightly smaller than experimentally obtained value of μ_{eff}. In general, an existence of SRO above the T_N can essentially lead to such larger value of experimental μ_{eff} [107], [272]. Therefore, the observed SRO in sufficiently high temperatures can elucidate the larger value of μ_{eff} in BMVO. The large negative value of Θ_{CW} indicates strong AFM interactions in BMVO. The larger value of frustration parameter f=Θ_{CW}/T_N~12.5 further suggests that BMVO is a highly frustrating system, which stems from the competing intrachain and interchain (consisting of AFM and FM) magnetic interactions [239].

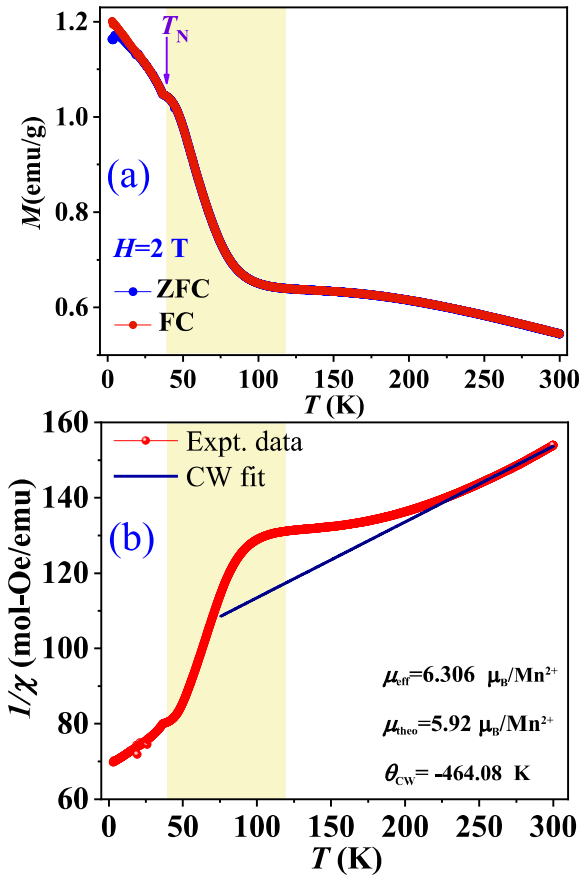

Fig. 6.6: (a) and (b) respectively represent the *M* (*T*) ZFC-FC curves at *H*= 2 T and the Curie-Weiss fit to the "1/χ *vs. T*" curve in the high-temperature range 240-300 K. The shaded region in yellow colour indicates the enhanced short-range ordering.

Fig. 6.7(a) and (b) demonstrate the M(H*)* curves at 2 and 300 K respectively. At 2 K, the magnetization attains a maximum value of ~0.258 μ_B/Mn^{2+} at the applied field of 7 T, which is very small as compared to the fully aligned saturation moment of Mn^{2+} ions ~5 μ_B. Moreover, the nonsaturating and merely linear nature of the M(H) curve even at a high field of 7 T at 2 K suggests the dominating AFM interactions in the system, thus supporting the NPD results. On the other hand, the M(H) curve at 300 K shows typical PM behavior, which is expected at temperatures well above its T_N.

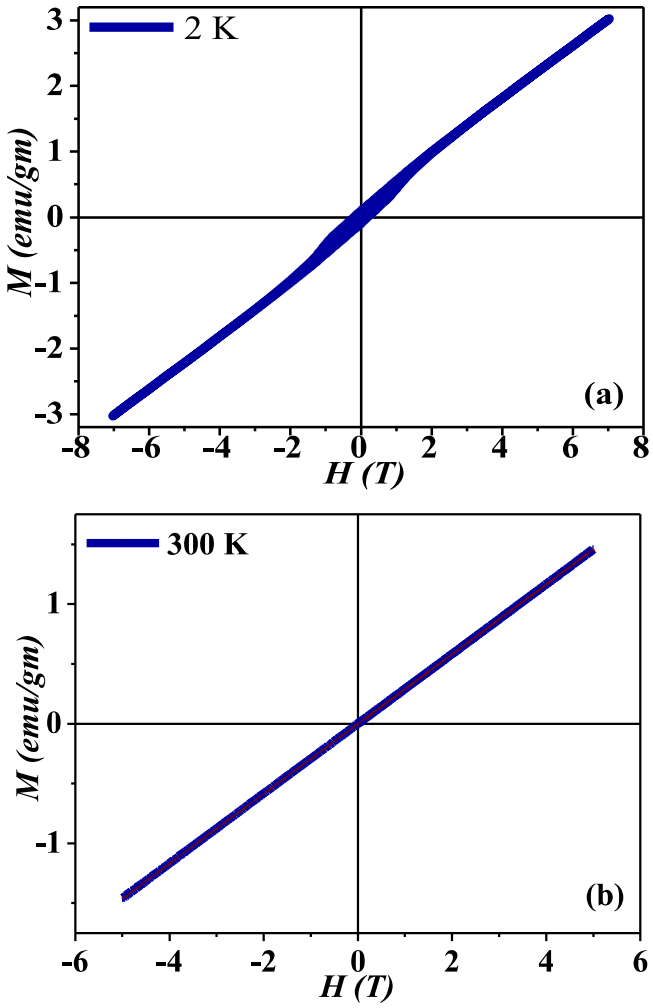

Fig. 6.7: (a) and (b) show *M(H)* curves at 2 K and 300 K, respectively.

6.4 Temperature-dependent Raman Study:

The diffraction techniques, i.e., neutron and XRD methods are useful in determining a global crystal structure of a system, whereas the Raman scattering spectroscopy comes with a unique capability that can sense a local modification in crystal symmetry, degree of cationic ordering, and SPC effect in a system. The unique exhibition of LRO in BMVO at a relatively high temperature (as compared to its other isostructural members in the $AM_2V_2O_8$ family) makes it a special system for investigating its lattice dynamics near T_N. Hence, we performed temperature-dependent Raman spectroscopy on BMVO and analyzed

the thermal evolution of its phonon behavior. Fig. 6.8 shows room temperature Raman spectra of the BMVO system. The insets of Fig. 6.8 display the Lorentzian fits the various observed Raman peaks in two different frequency ranges ω~300-500 cm^{-1} (intermediate range) and ω~750-920 cm^{-1} (high-frequency range). The spectra can be broadly divided into three bands centered near ω~200, 400, and 850 cm^{-1}, which are separated from each other by large gaps. The group theoretical symmetry analysis of the structure of BMVO having a space group $I4_1cd$ (No. 110) and a corresponding point group C_{4v} (4mm) predicts a total of 97 possible modes at its Γ-point of the Brillouin zone. These include 95 Raman active modes ($18A_1+19B_1+19B_2+39E$) of which 38 modes are exclusively Raman active ($19B_1+19B_2$), whereas 57 modes are simultaneously Raman and Infrared (IR) active ($18A_1+39E$). In addition, there are two acoustic modes (A_1+E).

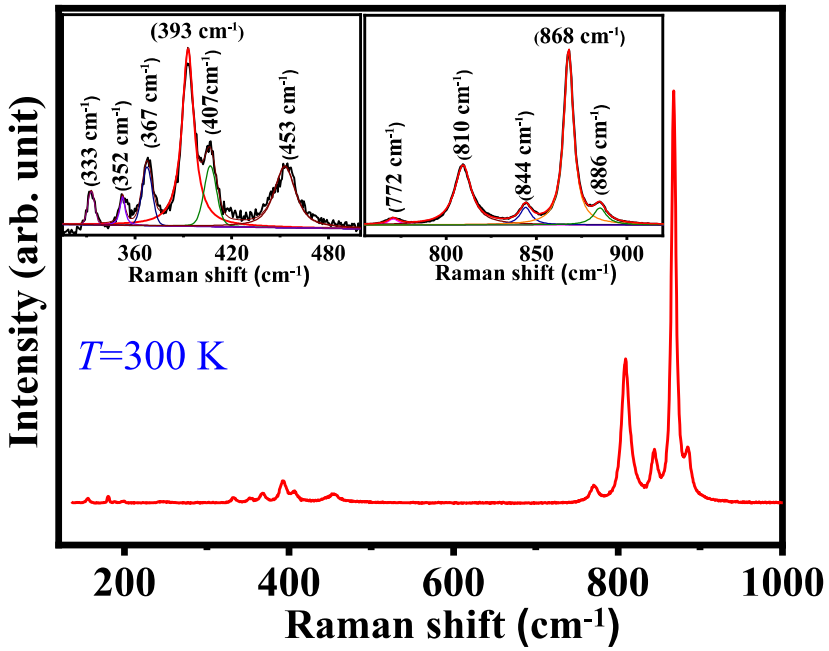

Fig. 6.8: Raman spectra at 300 K. Insets: Lorentzian fits of the observed peaks in the mid-frequency range (left) and high-frequency range (right).

The Raman spectra emanate from the various vibrations involving Ba^{2+}, Mn^{2+}, and O^{2-}, and also a rigid ionic complex $(VO_4)^{3-}$. However, the assignment of the observed Raman lines to various vibrational modes of the crystal is difficult without polarization-dependent measurements. Nevertheless, a qualitative discussion can still be made in this regard. In BMVO, the octahedral surrounding of each Mn^{2+} ion is coordinated by six O^{2-} ions, each of which belongs to six different rigid ionic complexes $(VO_4)^{3-}$ [137]. Thus, the internal vibrations of MnO_6 octahedra are entangled with the $(VO_4)^{3-}$ units. Such an ionic complex $(VO_4)^{3-}$ has a tetragonal environment with nine degrees of freedom as described by the T_d point group. The Raman modes appearing in the higher frequency range, i.e., ω~700-900 cm^{-1} are purely related to the symmetric and antisymmetric stretching vibrations of V-O valence bonds in the $(VO_4)^{3-}$ tetrahedron [137]. On the other hand, the Raman modes due to the symmetric, antisymmetric stretching, and/or bending vibrations in MnO_6 octahedron generally lie in the range of ω~300-700 cm^{-1} [161], [276], [277]. Moreover, the symmetric and asymmetric bending vibrations of the $(VO_4)^{3-}$ tetrahedron also lie in the frequency range of ω~300-450 cm^{-1} [137]. Thus, it is difficult to distinguish the individual Raman modes arising due to various vibrations from $(VO_4)^{3-}$ tetrahedron and MnO_6 octahedron. Therefore, in BMVO, the Raman modes observed in the range of ω~330-460 cm^{-1} can be attributed to the vibrations of MnO_6 octahedron as well as the bending vibrations of the $(VO_4)^{3-}$ tetrahedron, which is also interlinked with each other, as previously mentioned. Furthermore, the Raman modes observed at the lower frequency, i.e., ω<300 cm^{-1} can be attributed to the lattice modes, which comprise translational and librational vibrations of the heavier cations (Ba, Mn, V) [161].

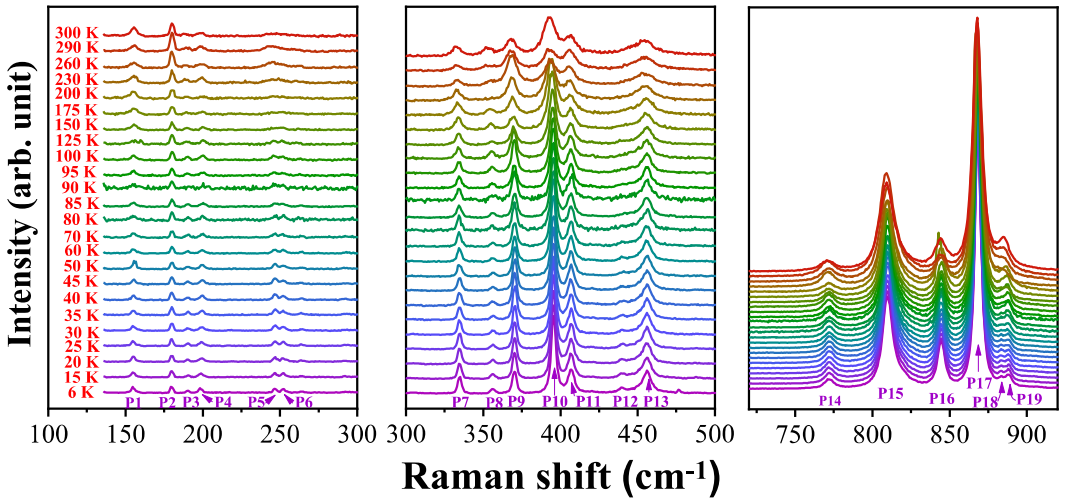

Fig. 6.9: Raman spectra at various temperatures in three different frequency ranges: 100-300 cm^{-1}, 300-500 cm^{-1}, and 720-920 cm^{-1}.

Fig. 6.9 shows temperature-dependent (6-300 K) Raman spectra in three different frequency ranges, viz., low-frequency range (ω~100-300 cm^{-1}), mid-frequency range (ω~300-500 cm^{-1}), and high-frequency range (ω~720-920 cm^{-1}). At the lowest temperature (6 K), a total of 19 Raman modes are clearly observed, which have been denoted as P1-P19 (Fig. 6.9). All the Raman spectra show similar patterns throughout the temperature range of interest. However, during cooling, as the temperature crosses near 125 K, a peak splitting occurs near 250 cm^{-1}, thus leading to the formation of two new Raman modes P5 and P6, as evident from Fig. 6.9. Moreover, another Raman mode (just above P17 mode) lying around ω~885 cm^{-1} at 300 K shows peak-splitting into two peaks viz., as P18 and P19, as the temperature cools below nearly 100 K. A closer view of the aforementioned peak-splitting is shown in Fig. 6.10(a) and (b). It can be reiterated that the magnetization, as well as NPD data, also indicated a sudden rise of SRO roughly around 100 K. However, as there is no global structural change observed in the NPD study, thus, the observation of the peak-

splitting into P5-P6 and P18-P19 modes (at temperatures in the vicinity of the enhanced SRO region) can be presumably attributed to a local structural distortion, which appears to have a close-correspondence with the rise of SRO in the system under study. A structural distortion can essentially alter the local structural symmetry, thus giving rise to an altered phonon spectrum [278]. In fact, the observation of an appearance of new Raman modes (near the onset of an SRO state) due to a local structural distortion induced by an SRO state was recently reported in a 15R-type $BaMnO_3$ compound [278]. However, further study of BMVO using a high-resolution synchrotron XRD measurement may be helpful to get an unambiguous explanation of the observed phenomena.

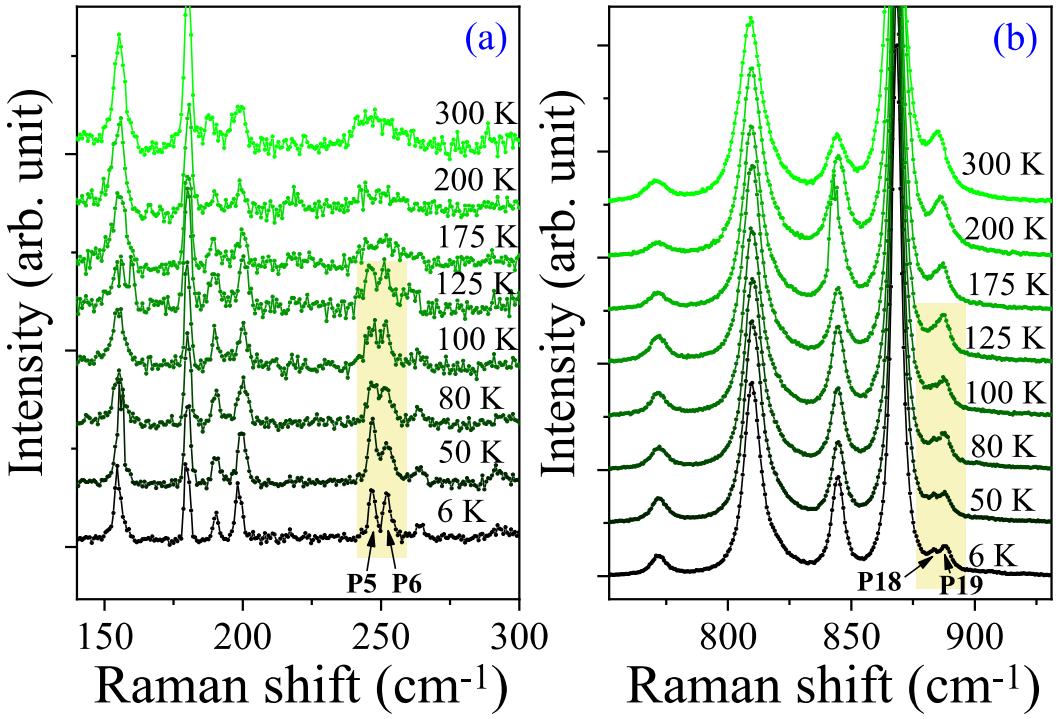

Fig. 6.10: A closer view of the Raman spectra at some selected temperatures near the peak-splitting of P5-P6 and P18-P19. For the peaks P5-P6, the peaks split in the vicinity of 125 K, whereas for P18-P19 peaks, the peak-splitting commences around temperatures below 100 K.

Furthermore, the thermal evolution of the various observed Raman peaks has been analyzed using Lorentzian fittings. For such analysis, we have selected the peaks with high or intermediate intensities, all of which appeared above ω~300 cm^{-1}. The thermal variations of the Raman shift (ω) and the corresponding FWHM or line-width of various Raman modes have been respectively shown in Fig. 6.11 and Fig. 6.12. In general, for the systems with magnetic atoms, thermal-variation of ω typically follows: $\omega(T) = \omega_0 + \Delta\omega_{latt}(T) + \Delta\omega_{anh}(T) + \Delta\omega_{e-ph}(T) + \Delta\omega_{s-ph}(T)$, where, ω_0 represents the frequency at an initial temperature T_0, $\Delta\omega_{latt}$ is related to the lattice contraction or expansion, $\Delta\omega_{anh}$ corresponds to the anharmonic contribution, $\Delta\omega_{e\text{-}ph,}$ and $\Delta\omega_{s\text{-}ph}$ respectively denotes the contributions from the electron-phonon coupling, and SPC [97]. Hence, if there is no structural change (local or global), SPC or electron-phonon coupling, or magnetostriction effect, ω usually follows the anharmonic equation, which is given as [98], [99]: $\omega_{anh}(T) = \omega_0 - C\left(1 + \frac{2}{e^{\frac{\hbar\omega_0}{2k_BT}} - 1}\right)$; where C represents an adjustable fitting parameter, $\hbar$ denotes the reduced Planck's constant, and k_B represents the Boltzmann's constant. According to the anharmonic equation, the $\omega(T)$ curves should exhibit a hardening (increase in ω) with decreasing temperature, thereafter attaining a lower temperature plateau. However, for the present case, the Raman modes in the mid-frequency range i.e., P13, P11, P10, P9, and P7 show a clear hardening behavior, at least down to 100 K. For the Raman modes in the higher frequency range, i.e., P17-P14, the change observed in ω for the entire temperature range is relatively smaller than that of Raman modes in the mid-frequency range. Moreover, the $\omega(T)$ curves in the high-frequency range do not show a systematic thermal variation (except for P14 mode) but display an overall increase at least down to T_N. Nevertheless, it can be noted that for at least two modes, such as P9 and P15, a noticeable anomalous phonon softening is clearly visible in the vicinity of T_N, which is shown in Fig. 6.11.

However, for the other modes, the anomalies are minimal or absent. The observed anomalous phonon softening is a typical feature of an SPC effect in a system showing an LRO [97], [121], [260], [278]. An anharmonic equation fit to the P9 mode shows a clear deviation below T_N (Fig. 6.11), thus suggesting the SPC effect. On the contrary, all the other modes including the P15 mode do not follow the anharmonic law even at high temperatures. The presence of strong SRO above T_N may lead to such violation of anharmonic behavior even at higher temperatures [278]. Therefore, it is plausible to elucidate the observed anomalous phonon softening in BMVO by a phonon renormalization caused by the strong spin correlations that develop as the LRO commences at T_N [97]. Moreover, small anomalies are also discernible near T_N in the FWHM variations (which are related to the phonon lifetime) with temperature, which is shown in Fig. 6.12. In general, FWHM of Raman modes remain unaltered due to a magnetostriction effect, but an anomaly in FWHM and $\omega(T)$ curves may signal an SPC effect in a system [121], [223], [278]. In fact, a magnetostriction effect manifests in the form of a remarkable anomaly in the unit-cell volume (V) at T_N [121], [223], [225]. For BMVO, the absence of such a remarkable anomaly in the $V(T)$ curve near T_N rules out the possibility of a magnetostriction effect in this system (Fig. 6.4(b). Therefore, an occurrence of the SPC effect in BMVO for at least two Raman modes, viz., P9 and P15 can be inferred. For the P9 mode (mid-frequency range), it involves MnO_6 vibrations, as previously mentioned. Thus, the stronger intrachain exchange interactions (AFM) along the Mn-Mn spin-chains appear to be the underlying origin for the observed anomalous phonon behavior in P9 mode (as in a spin-chain, two nearest neighbor Mn ions are connected by the edge-sharing of their two respective MnO_6 octahedra). On the contrary, the P15 mode lies in the high-frequency region, which involves internal stretching vibrations of the $(VO_4)^{3-}$ units (V-O bonds). The interchain exchange interactions (FM or AFM depending on the Mn ions lying in different

ab planes) in BMVO occur via the weaker exchange pathways of Mn-O-V-O-Mn (i.e., it gets mediated by the VO_4 units). Therefore, as the LRO sets in the system BMVO below T_N, a phonon renormalization may occur in P15 mode due to the weaker interchain magnetic exchange interactions, thus manifesting as an anomalous phonon softening of this mode. However, detailed lattice dynamics calculations and temperature-dependent polarized Raman spectroscopy study may further help in getting more insights into the mechanism of the SPC effect in BMVO. Nevertheless, the reports on the SPC effect in a spin-chain compound are very rare, thus the present observation of SPC in BMVO renders it among the rare materials.

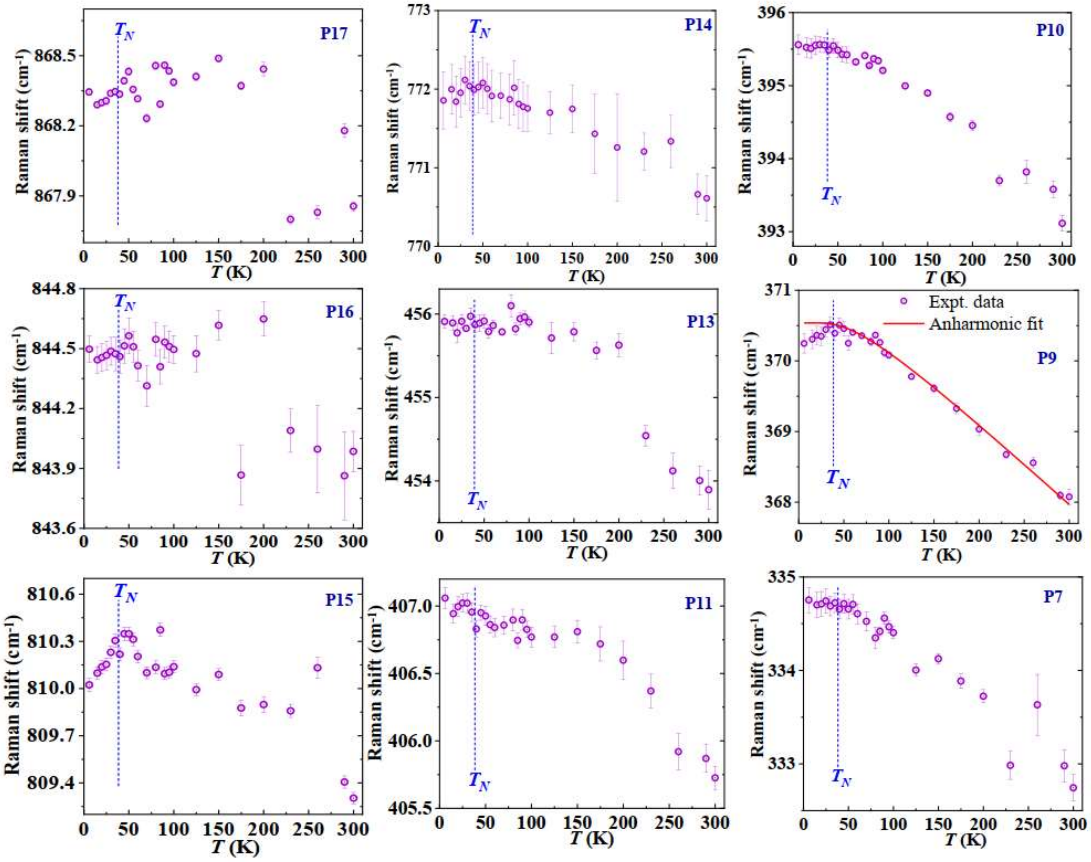

Fig. 6.11: Thermal variation of Raman shift for various Raman modes. For P9 mode, a deviation from the anharmonic fit below T_N is demonstrated.

Moreover, in the FWHM variations of various Raman modes and also in the *ω(T)* curves for a few Raman modes, anomalies near 250 K can be noted (our repeated Raman measurements also showed similar results). As mentioned earlier, the *V*(*T*) curve deviated from the thermal relaxation behavior above 250 K. Thus, an occurrence of a local structural change near 250 K can be assumed, which may cause the aforementioned anomalies. However, a high-resolution synchrotron study is needed to confirm this assumption.

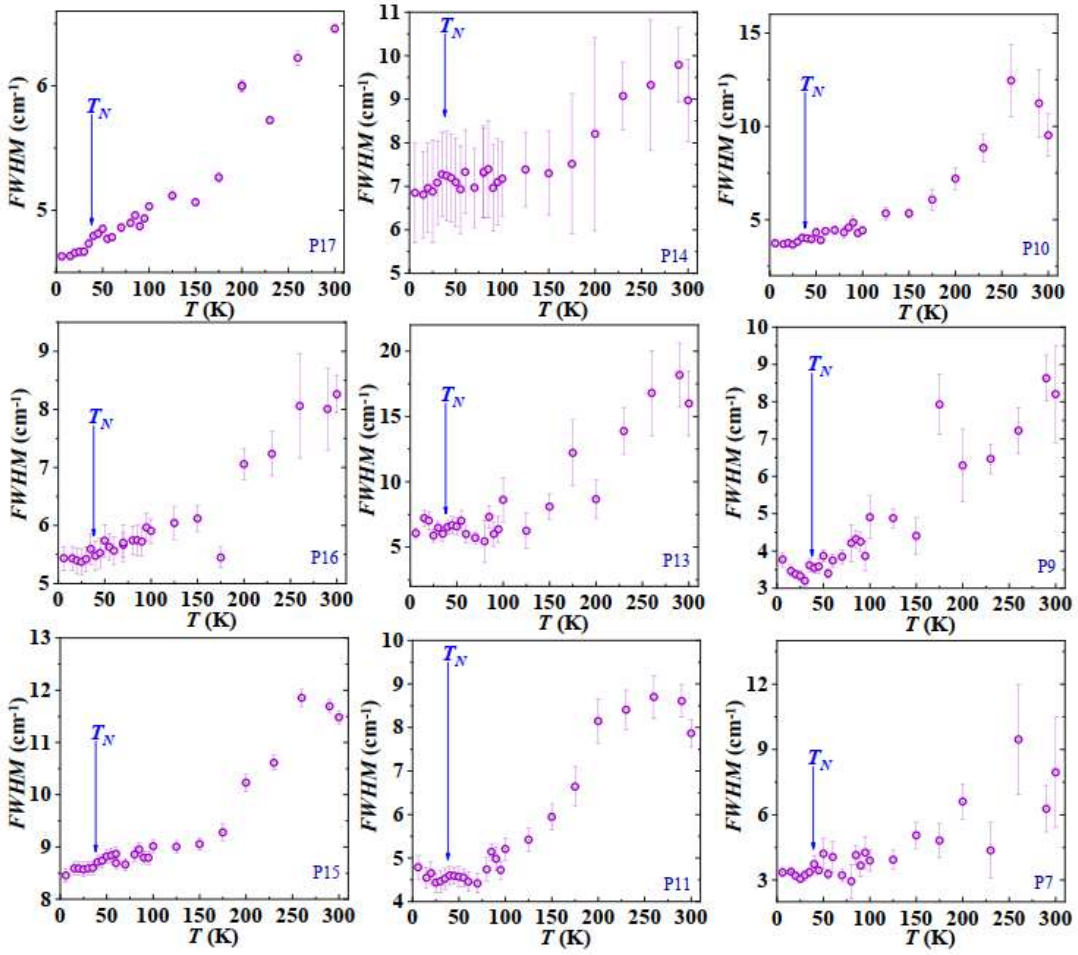

Fig. 6.12: The temperature dependence of FWHM of various Raman modes.

6.5 Electronic density of states (DOS) analysis by density functional theory:

We also carried out a detailed DFT based on *ab initio* calculations of BMVO to gain a deep insight into its electronic band structure and magnetic spin properties. The atomic positions, cell volume, and cell shape have been relaxed while keeping the crystal symmetry $I4_1cd$ unchanged. The PAW method is considered as the basis sets for Ba, Mn, V, and O; whereas the cut-off value was set as 400 eV. The GGA-PBE exchange-correlation functional is used for the calculations.

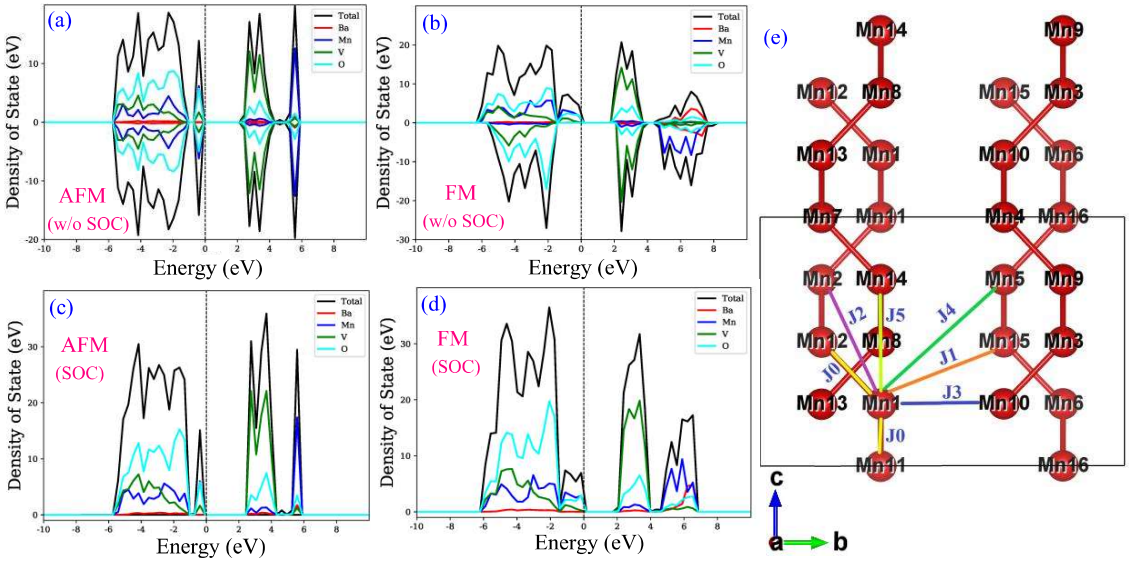

Fig. 6.13: DOS including TDOS and PDOS as obtained from the DFT calculations for (a) AFM and (b) FM spin configuration without considering the SOC. The calculated DOS for the AFM and FM spin configurations with SOC is shown in (c) and (d) respectively. The black line shows the TDOS, whereas the PDOS for different elements is shown in coloured lines. (e) shows the four screw-chains of Mn^{2+} ions in a unit-cell, wherein various exchange interaction interactions (J_0-J_5) between various Mn^{2+} ions (viz., Mn1-Mn16) are shown.

The Hubbard-U values of 5 and 3.5 eV respectively for atoms Mn and V have been employed, which can include the electron-correlation interaction in our system. After getting the structural and electronic convergence, the electronic properties in terms of the TDOS and the PDOS have been analyzed, wherein the original DOS has been decomposed into the DOS of individual elements. The calculations are carried out both for the AFM (considering the AFM coupling among the nearest neighbor Mn ions) and FM couplings among the Mn spins. Fig. 6.13(a) and (b) demonstrate the TDOS (black solid line) along with the PDOS (colored lines as indicated) for respective elements (Ba, Mn, V, and O) of BMVO for the AFM and FM spin configurations respectively, for the without SOC consideration. For the AFM case, for both the up and down spin channels, a large gap between the occupied (below Fermi level [E_F]) and unoccupied DOS (above E_F) is observed. Moreover, no finite DOS is seen across the Fermi level (Fig. 6.13(a)). These features predict the insulating behavior of the system. In fact, our room temperature resistivity measurement also showed a highly resistive nature of the system. On the other hand, for the FM case, although a large gap is also seen in the down spin channel, a finite DOS is visible in the up-spin channel, thus suggesting a slightly metallic nature of the system. The total energies of the system for both the AFM and FM cases are summarized in Table 6.2. It is observed that the AFM spin configuration has lower energy than the FM spin configuration, thus predicting an energetically favorable AFM ground state in this system, which also corroborates with the experimental results.

Table 6.2: The total energy of BMVO using different spin configurations without SOC and with SOC considerations.

Spin configuration	Total energy (eV)
FM without SOC	-765.95513
FM with SOC	-767.89258
AFM without SOC	-766.55335
AFM with SOC	-768.29068

Furthermore, the DOS results with the SOC considerations for the AFM and FM cases are shown in Fig. 6.13(c) and (d) respectively. It is observed that for the AFM case, the large gap in the DOS is still present after the application of SOC, while a slight increase in the gap can be noted. On the contrary, for the FM case, a sizeable DOS can still be observed across the E_F, which is not consistent with the highly insulating nature of the system. The total energy of the system after the application of SOC remains lower for the AFM case than that of the FM case. Thus, suggesting an AFM ground state of the system with insulating nature. For all the above cases, a substantial hybridization between the Mn3d-O2p states and a smaller but finite hybridization between the V3d-O2p states are visible in the occupied DOS near E_F, thus providing exchange pathways for the stronger intrachain and weaker interchain magnetic interactions among Mn ions.

6.6 Theoretical estimation of various magnetic exchange interactions:

In a screw-chain compound, the magnetic exchange interactions (J) are very important parameters that eventually decide the magnetic properties of that system. Therefore, it may be interesting to theoretically estimate various intrachain and interchain exchange interactions occurring in BMVO. In the present system, the experimental results suggested the presence of dominant AFM interactions. The spin-exchange interactions of a magnetic solid system can be modeled with exchange constants J_{ij} between spins $\widehat{S_i}$ and $\widehat{S_j}$ at sites i and j respectively, by the spin Hamiltonian,

$$\widehat{H} = -\sum_{j<j} J_{ij} \widehat{S_i} \cdot \widehat{S_j} \qquad 6.2$$

Where, J_{ij} is the spin exchange parameter for the spin exchange interaction between the spin sites i and j in BMVO, whereas $\widehat{S_i}$ and $\widehat{S_j}$ are the spin angular momentum operators at the spin sites i and j, respectively. In BMVO, both the Mn sites have $\left|\widehat{S_i}\right| = \left|\widehat{S_j}\right| = S = \frac{5}{2}$. A number of collinear AFM spin configurations can be used to estimate various exchange

interactions. In this case, various J between different Mn spins can be roughly estimated using a number of collinear AFM spin configurations by mapping BMVO to the aforementioned spin model. However, the various AFM configurations should be carefully chosen so that they are linearly independent and thus, the estimation of J is done for some specific bonds, including intrachain and interchain Mn spins [279]. The various exchange interactions (J_0-J_5) among different Mn ions, which have been estimated are indicated in Fig. 6.13(e). The corresponding pair distances (Mn-Mn bonds) are also shown in Table 6.3. For the calculations, we have calculated the energies of the FM and six different linearly independent AFM spin configurations, which are described in Table 6.4. Thereafter, the various exchange interactions (J_0-J_5) are expressed in terms of a set of linearly independent equations involving the relative energies (E_1 to E_6, which are calculated with respect to the total energy of FM configuration, i.e., E_0) of different aforementioned AFM spin configurations, which are given below:

$J_0=2[-(1/16)E_1 - (1/8)E_2 + (1/8)E_3 + (1/8)E_4 - (1/32)E_5 - (1/32)E_6]/S^2$,

$J_1=2[-(1/8)E_2 + (1/8)E_4]/S^2$,

$J_2=2[(3/32)E_1 + (3/8)E_2 - (1/4)E_3 - (5/16)\times E_4 + (1/64)E_5 + (3/64)E_6]/S^2$,

$J_3=2[-(1/16)E_1 - (1/8)E_2 + (1/8)E_3 + (1/8)E_4 - (1/16)E_6]/S^2$,

$J_4=2[-(1/32)E_1/32 - (1/16)E_2 + (1/16)E_3 + (1/64)E_5 + (1/64)E_6]/S^2$,

$J_5=2[(1/32)E_1 - (1/64)E_5 - (1/64)E_6]/S^2$,

The calculations suggested that the nearest neighbor intrachain exchange interaction, i.e., $J_0 \sim +2.999$ meV is the most dominant AFM interaction in BMVO, while the other magnetic exchange interactions (J_1-J_5) are much weaker as compared to J_0, which are evident from the Table-6.4. Therefore, the calculations indicate that J_0 plays a pivotal role in determining

the magnetic ground state in BMVO. Moreover, the next nearest neighbor intrachain interaction, i.e., J_2 also shows a sizeable FM exchange interaction of strength Contradistinctively, all the interchain interactions, viz., J_1, J_3, J_4, and J_5 are considerably weak. Thus, the results suggest that the spins in BMVO should stabilize in an AFM order, wherein the nearest-neighbor spins lie antiparallel to each other in a screw-chain, thus agreeing with the NPD results.

Table 6.3: Total energies of different AFM spin configurations. The signs + and – indicate spins with opposite directions.

Spin configuration	Spin orientations [Mn1, Mn2,…,Mn16]	Total energy (eV)
AFM1	[-, -, -, +, +, +, -, +, +, +, +, -, -, -, +, -]	-766.16383318
AFM2	[-, -, -, +, +, +, +, -, -, +, +, -, -, -, +, +]	-766.08467207
AFM3	[-, -, -, +, +, +, -, +, +, -, +, -, -, -, +, +]	-766.08810139
AFM4	[-, -, -, +, +, +, +, -, +, -, +, -, -, -, +, +]	-766.08366750
AFM5	[-, -, +, +, -, +, -, +, -, -, +, +, +, -, +, -]	-766.30485834
AFM6	[-, -, +, +, -, +, -, +, +, +, -, -, -, +, -, +]	-766.01579196

Table 6.4: The exchange parameters index, distances among chosen pairs, and numerical values of J_0-J_5 from the numerical fitting are shown.

Exchange parameters index	Pair distance (Å)	J values (meV)
J_0	3.00577	2.99929
J_1	5.15887	0.04018
J_2	5.23336	-0.57605
J_3	5.92971	0.10862
J_4	5.99899	-0.03351
J_5	6.03724	-0.03508

6.4 Conclusion:

A quasi 1D noncentrosymmetric spin-chain compound BMVO has been extensively studied by employing dc magnetization, NPD, XAS, and temperature-dependent Raman

spectroscopy measurements, which were accompanied by a comprehensive *ab initio* DFT calculations. Unlike most of the low-dimensional spin-chain compounds, BMVO exhibited a long-range AFM ordering at a sufficiently higher transition temperature, i.e., T_N=38 K, which was confirmed by the dc magnetization and NPD measurements. The NPD data analysis yielded a collinear AFM spin structure with the nearest-neighbor spins having an AFM-coupling along the screw-chain axis of the system, whereas the spin direction lies along the *a* or *b*-axis. The analysis further suggested that the AFM order in this spin-chain system develops with an unconventional critical exponent β=0.21. Moreover, a short-range magnetic ordering much above the T_N has been observed both from the dc magnetization and NPD studies, which is triggered by the intrachain interactions upon lowering the thermal energy. The temperature-dependent Raman spectroscopy measurements unraveled the exhibition of an SPC effect below T_N for at least two phonon modes. On the other hand, an unusual thermal evolution (such as violation of the anharmonic law and apparition of peak-splitting) of the Raman modes above T_N is observed, which seemingly emanates from the short-range magnetic ordering. Furthermore, the *ab initio* DFT calculations predicted an insulating AFM ground state of the system, which is in line with the experimental results. Theoretical calculations have also been done to estimate various possible exchange interactions in BMVO, which showed the nearest-neighbour intrachain exchange interactions are the most dominating interactions to stabilize the observed AFM ground state in BMVO.